Bond Performance of Ultra-High-Performance Concrete (UHPC) Under Flexural States

Yi Shao[1, *], Sarah L. Billington [2]

1. Postdoctoral Scholar, Dept. of Civil and Envir. Engineering, University of California, Berkeley, CA, USA
2. Professor, Dept. of Civil and Envir. Engineering, Stanford University, Stanford, CA, USA

[*]Corresponding author email: yishao@berkeley.edu

Abstract

Ultra-high performance concrete (UHPC) is a novel class of cementitious materials that shows ultra-high mechanical and durability performance, which is attracting attention for many applications. However, recent studies on steel-reinforced UHPC reveal that reinforcing bar strains may concentrate around the localized cracks, leading to early reinforcement fracture and low structural ductility. Understanding and simulating this steel concentration phenomenon requires information on the bond between steel reinforcement and UHPC. The bond performance of steel-reinforced UHPC has not been fully characterized, especially under flexural stress states. This study investigates the bond between steel reinforcement and UHPC using beam-end specimens. UHPC materials with two fiber volumes are considered: 2% and 1%. Results show that splitting cracks are well restrained in UHPC with both fiber volumes. The bond strength of UHPC is over four times higher than that of conventional concrete. This high bond strength makes UHPC beam-end specimens prone to cone-type failures, which should be avoided in bond characterization tests. A design method is developed to prevent cone-type failures in UHPC beam-end specimens. Microcomputed tomography (Micro-CT) scan results reveal that when casting-material flow is parallel to the longitudinal reinforcing bar, fibers are mostly parallel to the bar and a fiber-free zone with a thickness of around 1.9 mm exists around the bar.

Keywords: *UHPC, bond performance, fiber volume, cone-type failure, fiber distribution.*

1. Introduction

Ultra-high-performance concrete (UHPC) is a class of cementitious materials that is designed based on packing-density theory and thus features minimized porosity (Richard and Cheyrezy 1995). This minimized porosity grants UHPC materials high compressive strength (usually higher than 150 MPa) and high durability (very low to negligible chloride penetrability) (Haber et al. 2018). Steel fibers with a volume fraction of around 2% are usually added to mitigate the intrinsic brittleness of the UHPC matrix. The steel fibers also help UHPC achieve high tensile strength (Haber et al. 2018), shear resistance (Voo et al. 2010), and spalling resistance (Shao 2020). Recognizing the fiber contribution, UHPC is also often referred to as 'Ultra-high performance fiber-reinforced concrete (UHPFRC)'. These superior material properties make UHPC appealing for many applications, ranging from long-span bridges (e.g., Graybeal et al. 2020, Shao et al. 2018) to earthquake resistant structures (e.g., Wang et al. 2018, Zhang et al. 2020).

Shao and Billington (2019a) identifies two flexural failure paths for steel bar reinforced UHPC (R/UHPC): failure after crack localization or failure after gradual strain hardening. To demonstrate the differences between these two failure paths, Figure 1 presents the load-displacement responses and final crack patterns of two R/UHPC beams with similar total steel volume (Shao 2020): UHPC-vf2.0-ρ0.96 contains 2.0% steel fiber and 0.96% reinforcing bar, while UHPC-vf1.0-ρ2.10 includes 1.0% steel fiber and 2.10% reinforcing bar. For UHPC-vf2.0-ρ0.96, the specimen loses load capacity after cracks start localizing in the weakest

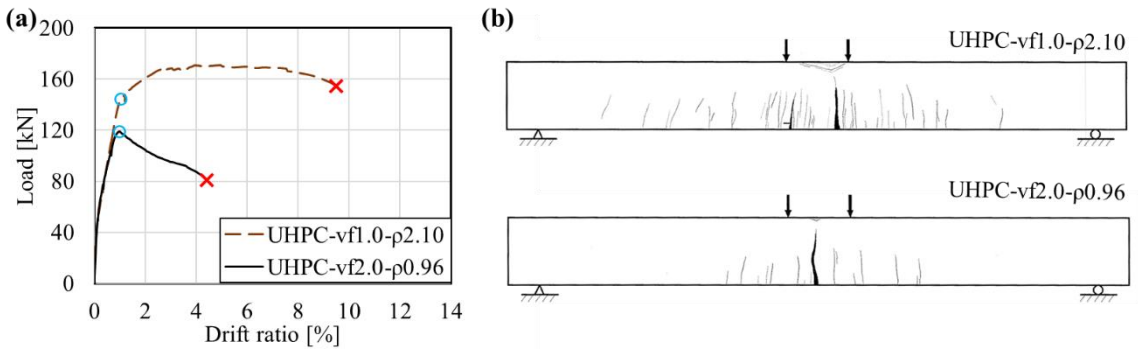

Figure 1. (a) load-displacement responses and (b) final crack patterns of UHPC-vf1.0-ρ2.10 and UHPC-vf2.0-ρ0.96. Note: in (a), '○': crack localization; '×': reinforcement fracture. Test details reported in Shao (2020).

plane and fiber-bridging capacity declines (i.e., crack localization). Subsequent steel strain-hardening cannot compensate for the fiber-bridging loss, which leads to the formation of only one localized crack and early steel fracture. This failure path is termed as 'failure after crack localization'.

Compared to UHPC-vf2.0-ρ0.96, UHPC-vf1.0-ρ2.10 contains less steel fibers (i.e., smaller fiber-bridging capacity) and more reinforcing steel (i.e., higher steel strain hardening capacity). Therefore, after crack localization, UHPC-vf1.0-ρ2.10 compensates for the fiber-bridging loss by gradual steel strain hardening, achieving a higher load capacity (Fig. 1a). The increased loading capacity allows the flexural stress to exceed the fiber-bridging capacity in other crack planes, leading to the formation of an additional localized crack and delaying steel fracture (Fig. 1b). This failure path is termed 'failure after gradual strain hardening'. A full discussion of these two failure paths and a failure path prediction method is presented in Shao and Billington (2019b).

Tension-stiffening tests of R/UHPC reveal that steel plasticity is restrained around the localized cracks, which indicates a high bond between the reinforcing steel and the UHPC matrix (Aghdasi and Ostertag 2020). This plasticity concentration leads to early steel fracture in R/UHPC if only one localized crack forms (e.g., UHPC-vf2.0-ρ0.96). Therefore, understanding the bond between steel reinforcement and UHPC is important for understanding and predicting R/UHPC structural behavior. While several studies have investigated the bond of R/UHPC, these studies have mostly been based on pullout tests (e.g., Yoo et al. 2014, Alkaysi and El-Tawil 2017, Khaksefidi et al. 2020), which do not represent the bonding behaviour in structural members due to the compression struts formed between ribs and rigid supports (ACI, 2003). Very limited information has been obtained about the bond of R/UHPC using a beam-type setup (Maya et al. 2013), which is recommended by ACI committee 408 for bond investigations in flexural stress state.

This study aims to investigate the bond performance of R/UHPC under flexure. Fifteen beam-end specimens were tested, including different unbonded lengths and two fiber volumes. A currently typical fiber volume (2%) is adopted, while a low fiber volume (1%) is also explored since a recent study shows that reducing the fiber volume to 1% improves R/UHPC structural ductility (Shao 2020). A simple method is proposed to choose the minimum unbonded length for R/UHPC beam-end specimens. Micro-CT scans are conducted to examine the fiber distribution around the reinforcing bar.

2. Experimental Program

2.1. Materials

This study adopted a commercial UHPC material, 'Ductal' from LafargeHolcim (US). This material included straight steel fibers with a diameter, length, and tensile strength of 0.2 mm, 13 mm, and 2160 MPa, respectively. According to the material-supplier-specified procedure, the material was mixed in a horizontal shear mixer and moisture cured until 3 days prior to the test date (28 days). The test reinforcing bar was an

A706 Grade 60 bar (Fig. 2a) with a nominal diameter (d_b), rib height, rib spacing, and relative rib ratio of 16 mm, 1.2 mm, 10.6 mm, and 0.096, respectively. The bar deformation was measured per ACI (2003).

Material characterization tests were conducted on the UHPC material with both fiber volumes (vf=1% or 2%) and the test reinforcing bar. Following ASTM C1856-17, the compressive strength and flexural behavior of the UHPC material were assessed using cylinder and unreinforced beam tests. Four specimens were tested for each fiber volume and test type combination. After end grinding, the cylinders had a diameter of 76 mm and a height of 141 mm. The average compressive strength was 174.0 MPa and 172.7 MPa for UHPC with 2% and 1% fiber volume, respectively. The unreinforced beams were 76 mm wide, 76 mm high, and 280 mm long. These beams were subject to third point bending with a span of 228 mm. Figure 2b presents the representative load-deflection responses for each fiber volume. Deflection-hardening and multiple cracking were observed in unreinforced beams with both fiber volumes. The tensile behavior of the test steel bar was assessed by uniaxial tension tests with a gauge length of 50 mm. Figure 2c presents the representative stress-strain responses of the test bar. More detailed discussions of the characterization test setup and results are available in Shao (2020).

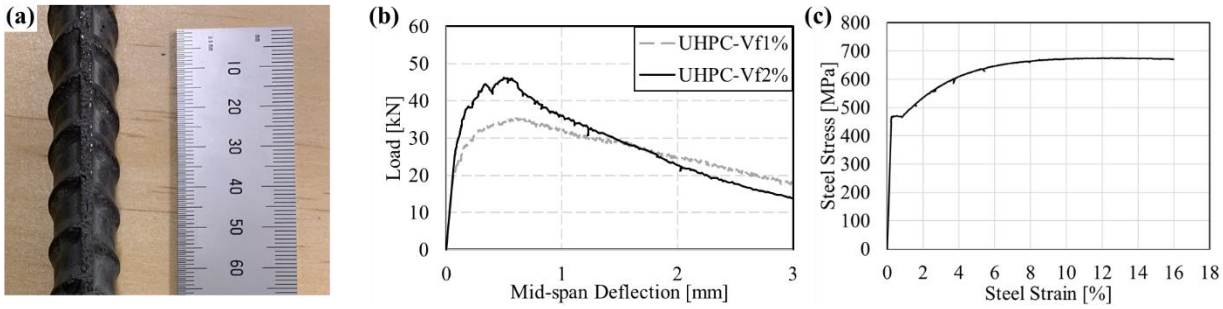

Figure 2. (a) test bar profile, and the material test results for (b) unreinforced UHPC beams and (c) test steel bar.

2.2. Specimen Design Test Setup

As recommended by ACI committee 408, beam-end specimens were adopted to investigate the bond-slip behavior of steel reinforcement embedded in UHPC flexural members. Figure 3 presents the beam-end specimen design, which has an embedded length of $3d_b$. The side cover thickness was 24 mm, which represents a typical value for UHPC applications. The loaded end of the test bar was debonded by a PVC pipe with a length of l_u to avoid a cone-type failure (ASTM A944-10). Five different unbonded lengths were investigated (Section 2.3) as establishing a method for choosing this unbonded length, l_u, was one of the goals of this study. As shown in Figure 3, two auxiliary steel bars and two stirrups were placed parallel to the test bar to limit flexural cracking and prevent shear failure.

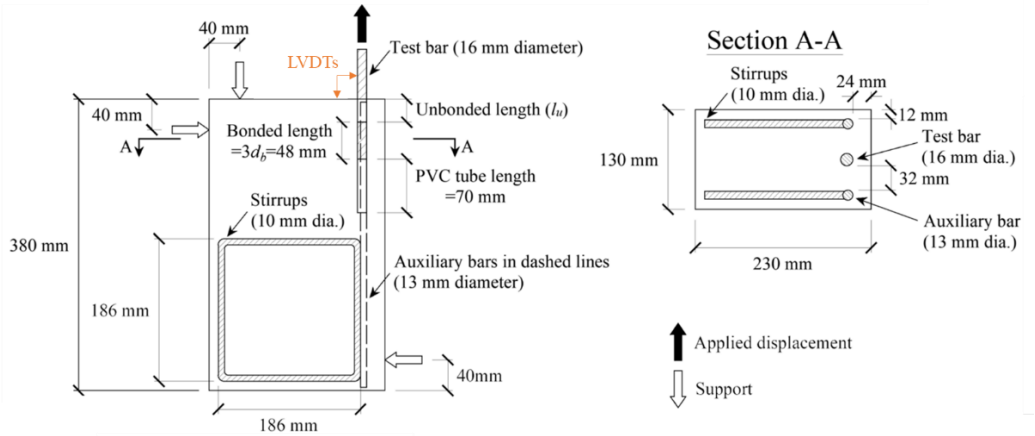

Figure 3. Schematic of the specimen design.

The material was placed from the unloaded end of the specimen and allowed to freely flow to the loaded end (Fig. 4a), which created a material flow parallel to the test bar. A parallel material flow is a representative flow condition in UHPC beam constructions. To understand the fiber distribution surrounding the bar, the test bar in one beam-end specimen was replaced by a 3D-printed polymer bar that had the same geometry and surface deformation as the test steel bar. Two cylindrical cores with a diameter and height of 44 mm and 100 mm was drilled and cut from this beam-end specimen (Fig. 4b). The cylinders were scanned using a Zeiss Xradia 520 Versa X-ray CT machine with a source power of 160kV at the Stanford Nano Shared Facility. The image resolution of the micro-CT scan was around 50 μm.

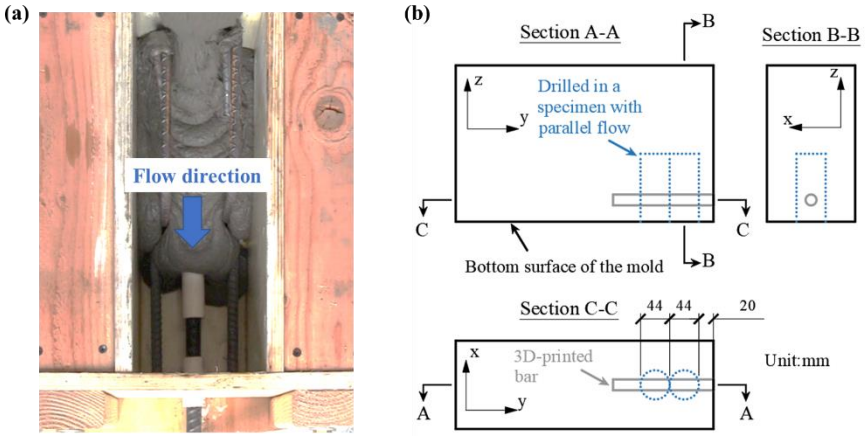

Figure 4. (a) Casting method and (b) core sample locations.

The test bar was uniaxially pulled by the actuator of a 245 kN MTS machine at a displacement-controlled rate of 0.008 mm/s. The specimen was restrained by steel rods against a rigid steel frame, resulting in the expected support forces shown in Figure 3. Two linear variable differential transformers (LVDTs) were clamped to the test bar, measuring the displacement of the clamping point against the top surface (Fig. 3). The bond slip of the bar was determined as the averaged LVDT readings minus steel deformation.

2.3. Test Matrix

Table 1 lists the test matrix. In the Phase 1 of the study, beam-end specimens with different fiber volumes (1% and 2%) and unbonded lengths (l_u from 1 cm to 5 cm) were tested. Based on the Phase 1 results (discussed in Section 3), the unbonded length was chosen as 3 cm. Three additional specimens with an unbonded length of 3 cm were tested for each fiber volume to demonstrate the repeatability of the results.

Table 1. Test matrix and results

Combination	V_f [%]	l_u [cm]	# Tests	u_{max} [MPa]	Failure Mode
UHPC-Vf1-1cm	1	1	1	19.0	Cone
UHPC-Vf1-2cm	1	2	1	21.0	Cone
UHPC-Vf1-3cm	1	3	4	29.9*	Confined splitting
UHPC-Vf1-4cm	1	4	1	26.7	Confined splitting
UHPC-Vf2-1cm	2	1	1	26.5	Cone
UHPC-Vf2-2cm	2	2	1	33.7	Confined splitting
UHPC-Vf2-3cm	2	3	4	32.6*	Confined splitting
UHPC-Vf2-4cm	2	4	1	43.1	Confined splitting
UHPC-Vf2-5cm	2	5	1	47.7	Pull-out

Note: V_f=fiber volume, l_u=loaded-end unbonded length (Fig. 3), u_{max}=Bond strength, *average of four tests.

3. Experimental Results and Discussions

Material test results are affected by the test specimen design and test setup, which should be optimized to match the conditions (e.g., stress fields and cracking) in the target applications. Phase 1 of this study optimizes the beam-end specimen design for assessing the UHPC bond performance in flexural members. The considered parameter is the loaded-end unbonded length (l_u) in Figure 3. The test results are presented in Table 1. The bond strength, u_{max}, is calculated as:

$$u_{max} = \frac{P_{max}}{\pi \cdot d_b \cdot l_{bond}} \quad (1)$$

where P_{max}=maximum load reached, l_{bond}=bonded length (48mm), d_b=bar diameter.

Figures 5a-b compares the beam-end test setup to a simply-supported beam test setup. The beam-end test setup in Figure 3 is rotated clockwise by 90 degrees. Figures 5c-e compares the crack patterns of UHPC-Vf2-3cm-#1 and UHPC-Vf2-5cm to the bottom crack pattern of a R/UHPC beam. Comparing Figure 5a to Figure 5b shows that beam-end tests match the flexural states of a simply-supported beam well: (1) the dominant crack plane in a simply-supported beam is simulated by the beam-end specimen face that is perpendicular to the pulling force, (2) the pulling force simulates the flexural tension force transferred by the longitudinal steel bar, and (3) the flexural compression force is simulated by the horizontal force that counteracts the pulling force.

There is one key difference between the beam-end specimen and a simply-supported beam: the loaded-end unbonded region in beam-end specimens. For bond-tests that involve pulling a bar from a free surface (both traditional pull-out tests and beam-end tests), a small portion of the bar near the surface is usually unbonded to avoid a cone-type failure as seen in Figure 6a (ACI, 2003). The length of this unbonded-length (l_u) should

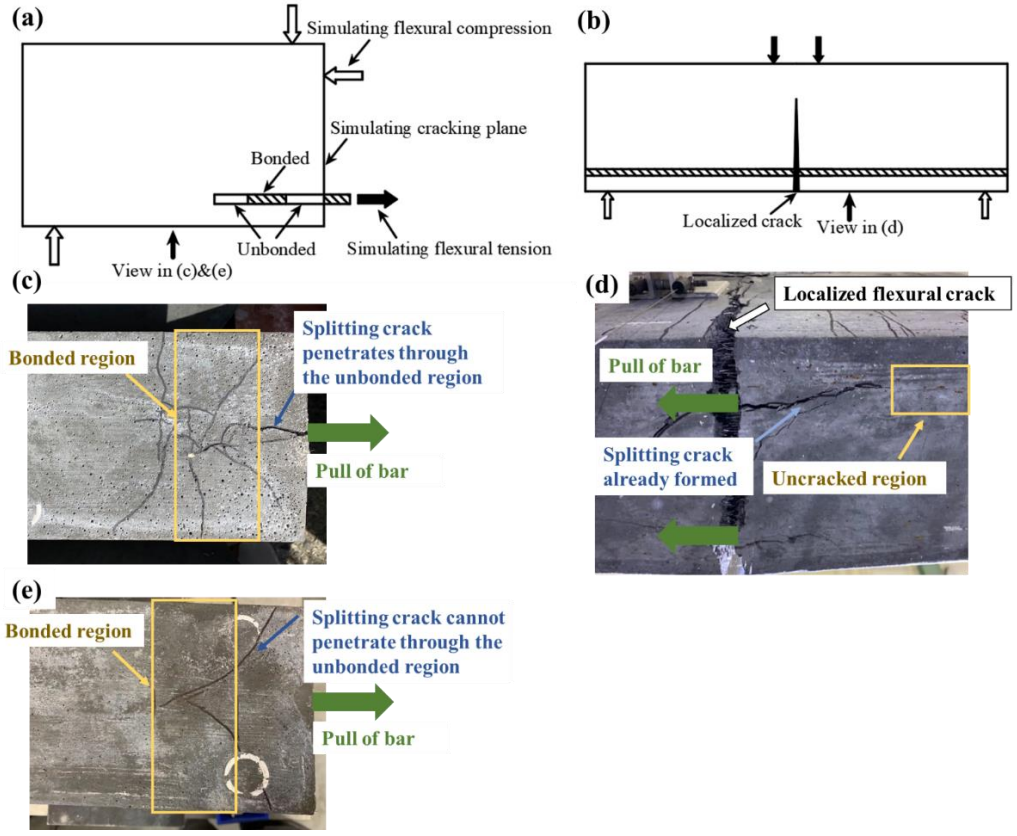

Figure 5. Comparison between beam-end tests and simply-supported beam tests using (a) schematic of a beam-end test setup, (b) schematic of a simply-supported beam test setup, (c) crack pattern of UHPC-Vf2-3cm-#1, (d) crack pattern of a simply-supported beam, and (e) crack pattern of UHPC-Vf2-5cm.

be reasonably chosen for two reasons. If the unbonded length is too short (e.g., UHPC-Vf2-1cm in Fig. 6a), a cone-type failure will form before the UHPC bond strength is reached. If the unbonded length is too long (e.g., UHPC-Vf2-5cm in Fig. 5e), the extra splitting resistance brought by the unbonded region would prevent the splitting crack from penetrating through the unbonded region, which violates the cracking pattern observed in UHPC beams (e.g., Fig. 5d). This high extra splitting resistance brought by the long unbonded length resulted in a pull-out type failure for UHPC-Vf2-5cm.

When the unbonded length is properly chosen, the beam-end specimens formed cracking patterns (Fig. 5c) that matched the flexural beam (Fig. 5d). These specimens formed multiple flexural cracks due to the flexural stress state with splitting cracks penetrating through the unbonded region (Fig. 6c). Although splitting cracks were observed, R/UHPC bond failure is considered as a confined splitting failure defined in *fib* (2010). Since fiber-bridging resists the splitting crack opening, the bond failure was ductile, and the UHPC keys between steel ribs were sheared-off for all specimens (Fig. 6d) except the specimens that failed with a cone-failure (Fig. 6b). For normal concrete, the splitting failure is brittle and the concrete keys between steel ribs remain intact after failure (e.g., Deng et al. 2019).

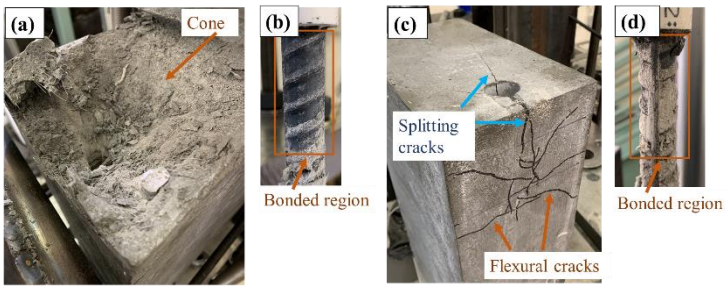

Figure 6. Photos of (a) the cone failure plane of P-Vf2-1cm, (b) the test bar of UHPC-Vf2-1cm, (c) crack patterns of UHPC-Vf2-3cm-#1, and (d) the test bar of UHPC-Vf2-3cm-#1.

Figure 7 presents the bond-slip responses of the specimens within combination UHPC-Vf1-3cm and UHPC-Vf2-3cm. For the bond strength associated with same fiber volume, the coefficient of variance is around 0.1, indicating a high repeatability of the test results. All specimens lost their bond strength quickly after the splitting crack initiated. However, the descending branch was gradual for both fiber volumes, which indicates that the fiber-bridging itself is able to resist unstable splitting opening. The average bond strength for specimens with 1% fiber volume is 8% lower than that with 2% fiber volume, possibly due to the weaker splitting resistance. Despite the differences caused by fiber volumes, the obtained UHPC bond strength (26.9-36.0 MPa) is at least 4 times higher than the bond strength observed in conventional concrete (e.g., 5.2-6.8 MPa, Bandelt and Billington 2016). This higher bond strength contributes to the plasticity concentration observed in R/UHPC tension-stiffening or beam tests, which leads to early steel fracture if only one localized crack forms (e.g., UHPC-vf2.0-ρ0.96 in Fig. 1).

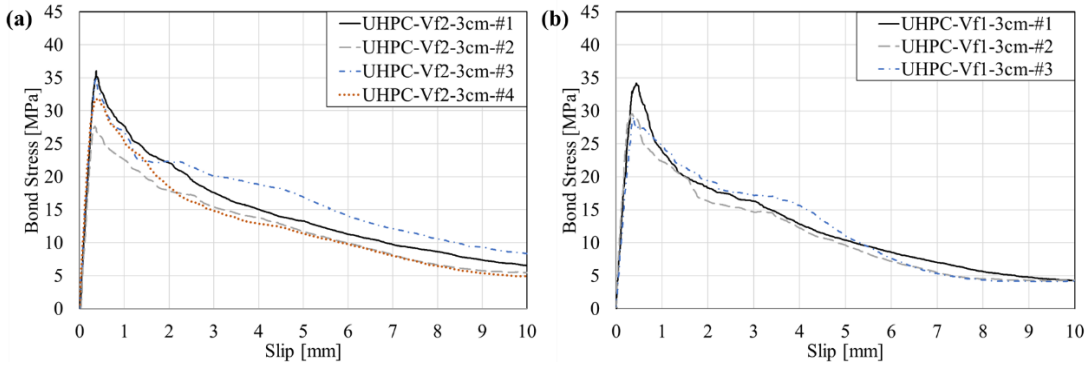

Figure 7. Bond-slip responses of specimens with (a) 2% fiber volume and 3 cm unbonded length and (b) 1% fiber volume and 3 cm unbonded length. Note: one specimen in UHPC-Vf1-3cm is not shown due to LVDT malfunction.

4. Choice of Minimum Unbonded Length

When designing a beam-end specimen, a method to choose the minimum unbonded length, l_u, is needed to prevent cone-type failure (Fig. 6a). Figure 8 presents the schematic of a hypothetical UHPC cone and its free body diagram, which forms the basis of the proposed cone-type failure prediction method. The center axis of the cone aligns with the test bar center line. The pulling force transferred by the bond is written as:

$$P_{pull} = u \cdot (H - l_u) \cdot \pi \cdot d_b \quad (2)$$

where u=bond stress, H=cone height. The vertical component of the cracking force can be written as:

$$P_{resistance} = P_{cr} \cdot cos\,\theta = \sigma_{cr} \cdot S_{surface} \cdot cos\,\theta \quad (3)$$

where σ_{cr}=cracking strength of the matrix, which is taken as 4.0 MPa based on the uniaxial tension tests reported in Shao (2020). θ is the angle as shown in Figure 8b. Based on experimental observations, θ ranges from $\frac{1}{6}\pi$ to $\frac{2}{9}\pi$. $S_{surface}$ is the surface area of the cone denoted by the red dashed lines in Figure 8b:

$$S_{surface} = \pi \cdot R \cdot \sqrt{H^2 + R^2} - \frac{(R^2 - L^2) \cdot \sqrt{H^2 + R^2}}{R} \cdot cos^{-1}\left(\frac{L}{R}\right) \quad (4)$$

where $R = H \cdot cot\,\theta$ is the cone base diameter; L=32 mm is the distance between the test bar center line and the side surface. Note that Equation 4 is the surface area of a cone that is cut by one side plane, which is of primary interests given the adopted cover thickness and bar diameter. For other cone states (e.g., the blue dotted line in Fig. 8a), the second term of Equation (4) shall be adjusted (e.g., L=R for the blue dotted line state in Fig. 8a). For a given combination of unbonded length, l_u, and hypothetical height, H, a cone-type failure is expected to occur when the following equation is satisfied.

$$P_{pull} = P_{resistance} \quad (5)$$

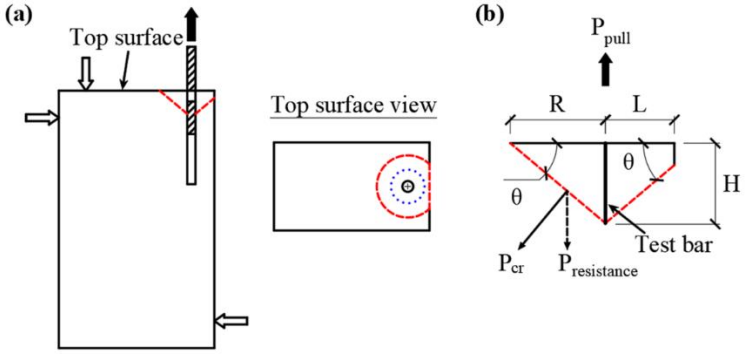

Figure 8. Schematic of (a) a hypothetical cone, and (b) free body diagram of the hypothetical cone.

The procedure to determine u_{cr} for a given unbonded length is illustrated in Figure 9. By solving equation (5) for all possible cone heights (l_u<H<l_u+bonded length), the critical bond stress, u_{cr}, that will cause cone-type failure can be determined. If u_{cr} is smaller than the expected bond strength, u_{max}, a cone-type failure will happen before bond failure.

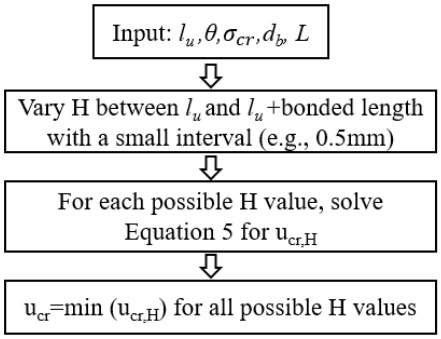

Figure 9. Procedure for determining u_{cr}.

Based on experimental observations, two θ values ($\frac{1}{6}\pi$ and $\frac{2}{9}\pi$) were checked, serving as an upper and lower bound of the possible θ values. Table 2 compares the calculated u_{cr} to the experimentally obtained u_{cr} for different l_u values. Table 2 shows that the prediction method described in Figure 9 is able to reasonably estimate the bond stress that causes a cone failure.

Table 2 Comparison between the predicted u_{cr} and the experimental u_{cr}

l_u [cm]	Predicted u_{cr} [MPa]		Experimental u_{cr} [MPa]
	$\theta = \frac{1}{6}\pi$	$\theta = \frac{2}{9}\pi$	
1	27.9	14.3	19.0, 26.5
2	42.1	22.8	21.0
3	56.4	29.6	NA*
4	71.0	36.5	NA*
5	86.0	44.0	NA*

Note: NA*=bond failure occurred instead of cone-type failure.

To simplify the calculations, a few assumptions are adopted with limitations introduced:

1. The bond stress, u, is assumed to be uniform along the bar. Since the bond is mainly transferred by the bearing against ribs, the bond force is actually not uniform. However, no information is available on the bond force that each rib can transfer to UHPC, and a uniform assumption is considered sufficient for prediction purposes.
2. The test bar is idealized as a line. This assumption introduces a small overestimation of the cone surface area by allowing the cone tip to exist. The cone actually intersects with the bar and does not have a tip as shown in Figure 8a. This assumption is adopted because it simplifies the calculations while introducing a relatively small error.
3. The real cone plane is idealized as a straight cone plane. In real specimens, the cone plane is affected by initial flaws and therefore is likely not a perfect straight plane (as shown in Fig. 6a). Also, the angle, θ, varies due to the flaw distributions and stress variations. Therefore, two different θ values were checked to explore possible upper and lower bounds of $u_{cr.}$

5. Fiber Distribution Surrounding the Bar

The fiber orientation was analyzed based on 2D image analysis. 2D CT images parallel to the x-z plane (i.e., perpendicular to the test bar, Fig. 4b) were first prepared at a 6.5 mm interval, which corresponds to half the fiber length. Then, a fiber orientation factor, α, was calculated based on the shape of intersecting fibers (Duque and Graybeal 2017, Kang and Kim 2011):

$$\alpha = \frac{1}{N}\sum_{i=1}^{N}\cos\theta_i = \frac{1}{N}\sum_{i=1}^{N}\frac{b_i}{a_i} \quad (6)$$

where N=number of fibers in a single image; θ_i is the estimated angle between the fiber axis and the vector normal to the image plane (Fig. 10a); a_i and b_i are the major and minor axis length of each intersected fiber footprint (Fig. 10a). Depending on the angles of the intersected fibers, α ranges from zero to one. If all fibers are perpendicular to the image plane (i.e., parallel to the test bar), then α will be one.

Figure 10b presents a representative 2D CT image. In Figure 10b, most fiber footprints (i.e., the small white shapes) had a small aspect ratio (i.e., close to a circle) and the calculated fiber orientation factor is 0.78, indicating that fibers are primarily parallel to the test bar and the global flow direction. These results confirm previous observations (e.g., Walsh et al. 2018, Zhou and Uchida 2017) that fibers are mostly parallel to the casting flow direction.

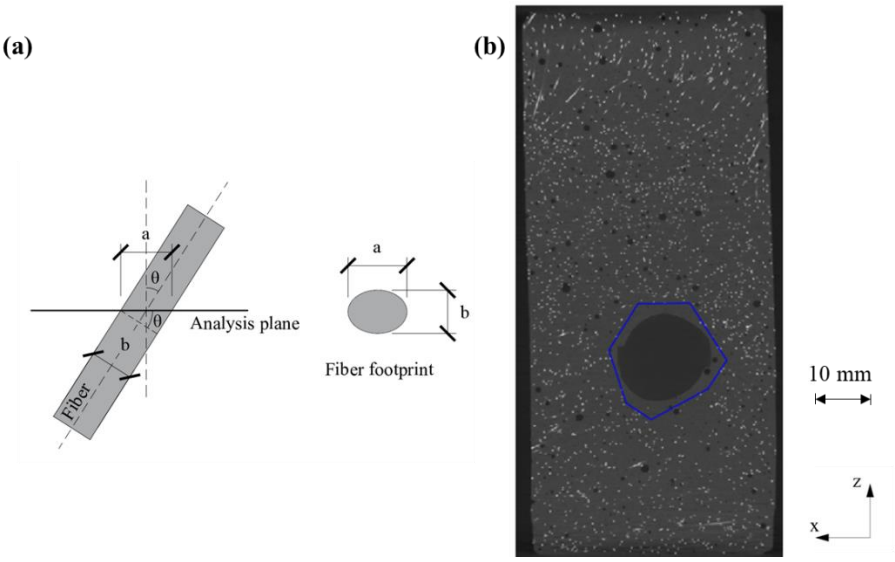

Fig. 10. (a) relationship between fiber aspect ratio (a/b) and fiber orientation; and (b) representative 2D CT image in X-Z plane.

Figure 10b also demonstrates that a fiber-free zone exists around the bar (enclosed by these blue dashed lines. The average thickness of the fiber-free zone is approximately 1.9 mm. Through numerical simulations, Bandelt et al. (2017) found that the material properties in the 2 mm interface zone near the steel bar significantly affect the bond-slip behavior of another high-performance fiber-reinforced cement-based material referred to as Engineered Cementitious Composites (ECC). Ongoing studies are investigating how this interface zone affects bond behavior in R/UHPC.

6. Conclusions

This study provides insights about R/UHPC bond behavior under a flexural stress state. The following conclusions can be drawn from this study:

- Beam-end specimens replicate the flexural stress states and crack patterns of flexural members well. An unbonded region should be provided near the loaded-end surface to avoid cone-type failure, and its length should be minimized to reduce the impact of the accompanying extra splitting resistance.
- A simple method for predicting a cone-type failure is developed. This method is intended to guide beam-end specimen design by providing a tool for choosing the smallest unbonded length that can avoid cone-type failures.
- Reducing the fiber volume from 2% to 1% lowers R/UHPC bond strength by 8%. Despite the differences introduced by different fiber volumes, R/UHPC exhibit a bond strength that is at least four times higher than that of conventional concrete.
- R/UHPC with both fiber volumes (1% and 2%) exhibit a confined splitting failure, showing that both fiber volumes are able to resist unstable splitting crack opening.
- Micro-CT scan results show that fibers are primarily parallel to the flow direction and a 1.9 mm-thick fiber-free zone exists around the bar.

Acknowledgements

The authors appreciate the material donation from LafargeHolcim (US) and Headed Reinforcement Corp, Fountain Valley, CA as well as the cylinder end-grinding service provided by the concrete material lab of California Department of Transportation, Sacramento. We gratefully thank John A. Blume Earthquake Engineering Center at Stanford University for the financial and technical support. We thank the lab help

from our undergraduate assistants: Sandro Boaro and Katie Tich. We appreciate the mixing and casting advice from Mr. Gregory Nault. We also thank Dr. Wilson Nguyen for helping review the paper.

References

ACI 408 (2003). Bond and Development of Straight Reinforcing Bars in Tension.

Aghdasi, P., and Ostertag, C. P. (2020). Tensile fracture characteristics of Green Ultra-High Performance Fiber-Reinforced Concrete (G-UHP-FRC) with longitudinal steel reinforcement. *Cement and Concrete Composites*, 103749.

Alkaysi, M., and El-Tawil, S. (2017). Factors affecting bond development between Ultra High Performance Concrete (UHPC) and steel bar reinforcement. *Constr. Build. Mater.*, 144, 412-422.

Bandelt, M. J., and Billington, S. L. (2016). Bond behavior of steel reinforcement in high-performance fiber-reinforced cementitious composite flexural members. *Mater. Struct.*, 49(1-2), 71-86.

Bandelt, M. J., Frank, T. E., Lepech, M. D., and Billington, S. L. (2017). Bond behavior and interface modeling of reinforced high-performance fiber-reinforced cementitious composites. *Cement and Concrete Composites*, 83, 188-201.

Deng, M., Pan, J., and Sun, H. (2019). Bond behavior of deformed bar embedded in Engineered Cementitious Composites under cyclic loading. *Constr. Build. Mater.*, 197, 164-174.

Duque, L. F. M., and Graybeal, B. (2017). Fiber orientation distribution and tensile mechanical response in UHPFRC. *Mater. Struct.*, 50(1), 55.

fib (2010). Fib Model Code for Concrete Structures 2010, *Ernst & Sohn*.

Graybeal, B., Brühwiler, E., Kim, B.-S., Toutlemonde, F., Voo, Y. L., and Zaghi, A. (2020). International Perspective on UHPC in Bridge Engineering. *Journal of Bridge Engineering*, 25(11), 04020094.

Haber, Z. B., De la Varga, I., Graybeal, B. A., Nakashoji, B., and El-Helou, R. (2018). Properties and Behavior of UHPC-Class Materials. *FHWA-HRT-18-036*.

Khaksefidi, S., Ghalehnovi, M., and De Brito, J. (2020). Bond behaviour of high-strength steel rebars in normal (NSC) and ultra-high performance concrete (UHPC). *Journal of Building Engineering*, 33, 101592.

Maya, L. F., Zanuy, C., Albajar, L., Lopez, C., and Portabella, J. (2013). Experimental assessment of connections for precast concrete frames using ultra high performance fibre reinforced concrete. *Constr. Build. Mater.*, 48, 173-186.

Richard, P., and Cheyrezy, M. (1995). Composition of reactive powder concretes. *Cement and concrete research*, 25(7), 1501-1511.

Shao, Y. (2020). Improving Ductility and Design Methods of Reinforced High-Performance Fiber-Reinforced Cementitious Composite (HPFRCC) Flexural Members. Ph.D., Stanford University, Stanford.

Shao, Y., and Billington, S. (2019a). Utilizing Full UHPC Compressive Strength in Steel Reinforced UHPC Beams. *Proc., 2nd Internation Interactive Symposium on UHPC. Albany, NY*.

Shao, Y., and Billington, S. L. (2019b). Predicting the two predominant flexural failure paths of longitudinally reinforced high-performance fiber-reinforced cementitious composite structural members. *Eng. Struct.*, 199, 109581.

Shao, Y., Shao, X., Li, L., and Wu, J. (2018). Optimum Combination of Bridge and Deck Systems for Superspan Cable-Stayed Bridges. *Journal of Bridge Engineering*, 23(1), 04017112.

Voo, Y. L., Poon, W. K., and Foster, S. J. (2010). Shear strength of steel fiber-reinforced ultrahigh-performance concrete beams without stirrups. *J. Struct. Eng.*, 136(11), 1393-1400.

Walsh, K., Hicks, N., Steinberg, E., Hussein, H., and Semendary, A. (2018). Fiber Orientation in Ultra-High-Performance Concrete Shear Keys of Adjacent-Box-Beam Bridges. *ACI Mater. J.*, 115(2).

Wang, Z., Wang, J.-Q., Tang, Y.-C., Liu, T.-X., Gao, Y.-F., and Zhang, J. (2018). Seismic behavior of precast segmental UHPC bridge columns with replaceable external cover plates and internal dissipaters. *Eng. Struct.*, 177, 540-555.

Yoo, D.-Y., Park, J.-J., Kim, S.-W., and Yoon, Y.-S. (2014). Influence of reinforcing bar type on autogenous shrinkage stress and bond behavior of ultra high performance fiber reinforced concrete. *Cement and Concrete Composites*, 48, 150-161.

Zhang, Z.-Y., Ding, R., Nie, X., and Fan, J.-S. (2020). Seismic performance of a novel interior precast concrete beam-column joint using ultra-high performance concrete. *Eng. Struct.*, 222, 111145.

Zhou, B., and Uchida, Y. (2017). Influence of flowability, casting time and formwork geometry on fiber orientation and mechanical properties of UHPFRC. *Cement and Concrete Research*, 95, 164-177.